Elastic behavior and pressure-induced structural modifications of the microporous Ca(VO)Si4O10 4H2O dimorphs cavansite and pentagonite

Elastic behavior and pressure-induced structural modifications of the microporous $Ca(VO)Si_4O_{10}\cdot 4H_2O$ dimorphs cavansite and pentagonite

ROSA MICAELA DANISI*[1)], THOMAS ARMBRUSTER [1)], ROSSELLA ARLETTI[2)], G. DIEGO GATTA[3)], GIOVANNA VEZZALINI[4)], SIMONA QUARTIERI[5)], VLADIMIR DMITRIEV[6)].

[1)]Mineralogical Crystallography, Institute of Geological Sciences, University of Bern, Freiestrasse 3, 3012 Bern, Switzerland

[2)]Dipartimento di Scienze della Terra, Università di Torino, via Valperga Caluso 35, Torino, Italy.

[3)]Dipartimento di Scienze della Terra, Università degli Studi di Milano, via Botticelli 23, Milano, Italy

[4)]Dipartimento di Scienze Chimiche e Geologiche, Università di Modena e Reggio Emilia, via S. Eufemia 19, Modena, Italy.

[5)]Dipartimento di Fisica e Scienze della Terra , Università di Messina, viale Ferdinando Stagno d'Alcontres 31, Messina S. Agata, Italy.

[6)]Swiss–Norwegian Beam Line at ESRF, BP220, 38043 Grenoble Cedex, France

*Corresponding author. E-mail address: rosa.danisi@krist.unibe.ch. Fax: +41316314273

ABSTRACT

The behavior of natural microporous cavansite and pentagonite, orthorhombic dimorphs of $Ca(VO)(Si_4O_{10})\cdot 4H_2O$, were studied at high pressure by means of in-situ synchrotron X-ray powder diffraction with a diamond anvil cell using two different pressure-transmitting fluids: methanol:ethanol:water = 16:3:1 (m.e.w.) and silicone oil (s.o.). *In situ* diffraction-data on a cavansite sample from Wagholi quarry, Poona district (India) were collected up to 8.17(5) GPa in m.e.w, and up to 7.28(5) GPa in s.o., showing similar compressional patterns in both the fluids. The high-pressure structure evolution was studied on the basis of structural refinements at different pressures: 1.08(5), 3.27(5) and 6.45(5) GPa. The compressional behavior is strongly anisotropic. When the sample is compressed in s.o. from P_{amb} to 7.28(5) GPa, the volume contraction is 12.2%, whereas **a**, **b** and **c** decrease by 1.6, 10.3 and 0.3%, respectively. The main

deformation mechanisms at high-pressure are basically driven by variation of the T-O-T angles. The L/S ratio of the longest to the shortest cross sections of the eight-membered rings varies from 1.74 at P_{amb} to 1.50 at 3.27(5) GPa. With increasing pressure, the shape of the rings becomes more rounded and in the last compression step, at 6.45(5) GPa, the eight-membered rings in the **a**-**c** plane enhance their circular shape with a L/S ratio of 1.25.

Powder diffraction data on a pentagonite sample from Wagholi quarry, Poona district (India), were collected up to 8.26(5) GPa in m.e.w and 8.35(5) GPa in s.o. Additional single-crystal X-ray diffraction experiments were performed in m.e.w. up to 2.04(5) GPa. In both cases, pressure-induced over-hydration was observed in m.e.w. at high pressure. The penetration of a new H_2O molecule leads to a stiffening effect of the whole structure and to a rearrangement of the H_2O molecule system, without additional distortion of the framework. Moreover, between 2.45(5) and 2.96(5) GPa in m.e.w., a phase transition from an orthorhombic to a triclinic phase was observed. In s.o. pentagonite also transformed to a triclinic phase above 1.71(5) GPa. The overall compressibility of pentagonite and cavansite in s.o. are comparable, with a volume contraction of 11.6% and 12.2%, respectively.

KEYWORDS: microporous materials, heteropolyhedral frameworks, cavansite, pentagonite, elastic behavior, pressure-induced hydration.

INTRODUCTION

Microporous heteropolyhedral frameworks [1] have recently attracted technological attention leading to a shift of interest from zeolites *sensu stricto* (tetrahedral frameworks with cation-exchange capacity and reversible dehydration) to zeolite-like structures (open-framework

materials with ion-exchange capacity). Natural microporous cavansite and pentagonite, dimorphs of $Ca(VO)(Si_4O_{10})\cdot 4H_2O$, have sparked our interest due to the technological potential of their porous framework made up by vanadyl-type pyramids connecting silicate tetrahedral sheets. In the last years, many studies addressing hydrothermal preparation procedures of new synthetic microporous vanadosilicates [2-4] aimed to optimize synthesis in order to obtain large quantities [5-6]. Such frameworks can fulfill many properties comparable to traditional zeolite structures such as microporosity, ion exchange and sorption applications. Moreover, the presence of transition metal ions in the framework makes these materials potentially usable for catalysis. Vanadium can adopt several oxidation states and vanadium silicates appear to be more stable than the corresponding phosphates [4]. In this light, the investigation of the thermo-elastic stability of vanadosilicates is crucial to evaluate their functionality for technical applications.

Non-ambient conditions can induce important structural changes in microporous materials, modifying physico-chemical properties and affecting their possible applications. Because of their applicative relevance, the thermal and baric stability of zeolites have been investigated extensively. Framework topology and extraframework content are crucial factors influencing structure deformation mechanisms not only upon thermal treatment but also under high-pressure conditions. Microporosity does not necessary connote high compressibility, as several zeolites are less compressible than other rock-forming minerals (for example α-quartz, [7]). Deformation mechanisms are governed by the topological configuration of the framework while the extraframework content influences the compressibility. The mechanism leading to topological changes in aluminosilicate frameworks can be described as tilting of rigid tetrahedra around O atoms [8-9]. Of particular interest, the high-pressure behavior of microporous materials can be affected by the nature of the pressure-transmitting medium used for the experiment. Using pore-penetrating pressure-transmitting media, it is possible to investigate pressure-induced over-

hydration (PIH) effects. In contrast, non-penetrating media are used to study compressibility, *P*-induced phase transitions, and amorphization. The most commonly used fluids for microporous materials are: methanol:ethanol (4:1) and methanol:ethanol:water (16:3:1) mix, glycerol and silicone oil. These pressure-trasmitting media have different freezing points and hydrostaticity as a function of pressure [10-11].

Our interest on the behavior of microporous materials with non-tetrahedral polyhedra at high pressure started after observing that the presence of octahedral Al in the framework of ALPO-34 leads to a stiffening of the framework upon compression if compared to SAPO-34 with tetrahedral Al [12]. Thus, the effect of the unusual presence of vanadyl-type square based pyramids on framework distortion and compressibility is of remarkable interest. In this light, our study represents the first investigation on high pressure behavior of heteropolyhedral vanadosilicate frameworks.

Cavansite, and its dimorph pentagonite, $Ca(VO)(Si_4O_{10})\cdot 4H_2O$, are the only known natural examples of microporous vanadosilicates. These minerals have been selected as representative of vanadosilicate frameworks for high-pressure study because of their large crystal size (mm range) and high crystal quality. The porous three-dimensional framework is built by tetrahedral sheets connected through VO_5 square based pyramids. The VO_5 pyramids are characterized by a short apical V-O bond of ca. 1.6 Å and four basal bonds of ca. 2.0 Å [13]. Pentagonite and cavansite are orthorhombic and characterized by undulating pyroxenoid-like $(SiO_3)_n$ chains. These chains are laterally joined into sheets parallel to the **a-c** plane but they are made up to arrange a different network of rings in the two structures. In cavansite, the tetrahedral sheets consist of four-fold and eight-fold rings, whereas in pentagonite there are only six-membered rings [13]. Moreover, in both dimorphic structures, adjacent chains have the tetrahedral apices pointing up and down along the **b** axis. Large cavities in the structure are decorated by Ca and H_2O molecules as

extraframework components. The cavansite framework can be compared to that of gismondine, $Ca[Al_2Si_2O_8]\cdot 4H_2O$ and amicite, $NaK[Al_2Si_2O_8]\cdot 2.5H_2O$. In gismondine and amicite (**GIS** frameworks), the same network of four- and eight- fold rings as in cavansite is present. In gismondine, adjacent tetrahedral layers are linked directly to each other to form a three-dimensional aluminosilicate network [14] and not via vanadyl-type VO_5 square pyramids as in cavansite. In cavansite, direct connection of the (010) tetrahedral layers without the VO_5 group would produce a tetrahedral network topologically identical to that of gismondine.

The behavior of cavansite and pentagonite upon heating appears to be zeolitic in character. [15-19]. More recently, *in situ* single-crystal X-ray dehydration experiments on cavansite and pentagonite were conducted to highlight the relationship between stepwise dehydration and framework distortion [20-21]. The presence of H_2O molecules in the porous framework is usually the promoter of structural modifications in response to the applied temperature. Moreover, the Ca coordination number coupled with the different flexibility of the frameworks seems to be responsible for either phase transitions or structural collapse in pentagonite and cavansite, respectively. The dehydration dynamics of cavansite were probed also by *in situ* synchrotron powder diffraction [22]. The knowledge of the pressure-induced structural modifications in cavansite is limited to a Raman spectroscopic study by Ravindran et al. [23]. Structural studies aiming to understand high-pressure behavior of pentagonite are missing.

EXPERIMENTAL METHODS

X-ray powder diffraction at ambient pressure

Cavansite and pentagonite crystals from Wagholi, Poona district, Maharashtra, India were selected and each sample was finely ground in a mortar to obtain a powder. The powders were

placed into 0.3 mm glass capillaries and mounted on a goniometric spinning head. The X-Ray Powder Diffraction (XRPD) experiments were performed at the SNBL (BM01A) beamline at ESRF (European Synchrotron Facility, Grenoble, France) with fixed wavelength of 0.682534 Å. All data were collected in the Debye-Scherrer geometry with a Dectris Pilatus2M detector. The sample-to-detector distance and the detector parameters were calibrated using a LaB_6 NIST reference powder sample. One-dimensional diffraction pattern was extracted by integrating the two-dimensional image using the program FIT2D [24]. Rietveld profile fitting in the 2 - 45° 2θ range was executed using the GSAS package [25] with the EXPGUI interface [26]. Initial structural models for cavansite and pentagonite were those of Evans [13] but, for cavansite, the standard space-group setting *Pnma* was preferred to *Pcmn* reported by Evans [13], requiring interchange of **a** and **c**. The background was fitted by a Chebyshew polynomial with 15 coefficients. The pseudo-Voight profile function [27] was used with refined Gaussian (GW) and Lorentzian (LX) terms and a cut-off was applied for the peak intensity. The scale factor and 2θ-zero shift were refined. Soft-restrains were applied to the T-O distances [Si-O = 1.58(3)-1.66(4)] and the weight was gradually decreased during the refinement up to a final value of F=10. Other soft-restrains were applied for the V-O [one short bond V-O = 1.59(1) and four V-O = 1.98(1)-2.00(1)]. The isotropic displacement parameters were constrained to a common value for the two tetrahedral sites. A second value was assumed for all framework oxygen-atoms, whereas the oxygen atoms at H_2O sites were constrained to a third value. The unit-cell parameters were refined in all cycles.

X-ray powder diffraction at high pressure

The *in situ* high pressure X-ray powder-diffraction data were collected using an ETHZ modified Merril-Basset diamond anvil cell (DAC) [28] with flat culets of diameter 600 μm. The

samples were loaded into a hole of 250 μm in diameter drilled in stainless steel gaskets pre-indented to 60-80 μm thickness. In order to compare the compressibility behavior of cavansite and pentagonite, different experiments were performed using two different pressure-transmitting media: methanol:ethanol:water 16:3:1 (m.e.w.) as nominally penetrating *P*-transmitting medium, and silicone oil (s.o.), as non-penetrating *P*-transmitting fluid. Pressure was measured before and after the data collection at each pressure using the ruby fluorescence method [29] on the non-linear hydrostatic pressure scale [30].

Cavansite

The pressure range investigated for the cavansite experiment in m.e.w. was from 0.01(5) to 8.17(5) GPa, whereas in s.o. from 0.01(5) to 7.28(5) GPa. Some patterns were collected in decompression down to room pressure (labeled (rev) in tables and figures).

In both the experiments, about 20 data points at different pressures were collected. Selected integrated patterns are reported in Figure 1a and 1b. For cavansite in m.e.w., the experiments up to 0.52(5) GPa allowed structural refinements to converge successfully, whereas at higher pressure only the unit-cell parameters were refined by the Rietveld method in the 2-23° 2θ range. The lattice parameters from 6.71(5) to 8.17(5) GPa in m.e.w. were determined through Le Bail full-profile fit [31]. The crystal-structure refinement of cavansite in s.o. was performed by the Rietveld method in the 2-32° 2θ range for all the data points up to 6.45(5) GPa. Differently from that usually reported, the structural refinement of cavansite in s.o. at high pressure was possible, in contrast to data collected in m.e.w. as pressure medium. The integration procedure and refinement strategy is comparable to those employed for data analysis at ambient pressure. The background was fitted by a Chebyshew polynomial with 21 coefficients. The pseudo-Voight profile function was used with refined Lorentzian (LX) term. The unit-cell parameters, scale

factor and 2θ-zero shift were refined in all cycles. The strategy applied for the soft-restrains to the T-O, V-O and Ca-O distances was the same as that at ambient pressure conditions.

Pentagonite

The pressure ranges adopted in the experiments on pentagonite were from P_{amb} to 8.26(5) GPa and P_{amb} to 8.35(5) GPa for m.e.w. and s.o., respectively. Selected integrated patterns are reported in Figure 2a and 2b. For pentagonite in m.e.w., the experiments up to 2.45(5) GPa allow structural refinements to converge successfully, whereas at higher pressure only the unit-cell parameters were refined by the Le Bail method [31] in the 2-23° 2θ range. Even though both experiments evidenced the occurrence of PIH, we discuss here in detail only the single crystal data (see below), being of higher quality with respect to powder diffraction. The quality of data obtained from the pentagonite experiment in s.o. is very low, probably in response to the non-hydrostatic compression in this medium already at $P>$ 1 GPa [10]. The lattice parameters from P_{amb} to 0.64(5) GPa in s.o. were refined by the Rietveld method, whereas at higher pressure the cell dimensions were determined through the Le Bail method [31]. Nevertheless, the quality of the Le Bail fit was poor, due to peak broadening at high pressure.

X-ray single-crystal diffraction on pentagonite

One prismatic crystal of pentagonite, free of defects or twinning under the transmitting polarized light microscope, was selected for the high-pressure (H*P*) X-ray diffraction experiments. Diffraction data were first collected at room conditions, with the crystal in air, with an Oxford Diffraction - Xcalibur diffractometer equipped with CCD, using graphite monochromatized Mo*K*α-radiation, operated at 50 kV and 35 mA. The distance between the crystal and the detector was set to 80 mm, as used for the H*P* experiments. Integrated intensities

were then corrected for Lorentz-polarization (Lp) and for absorption effects (by Gaussian integration based upon the shape and dimensions of the crystal), using the CrysAlis package [32]. After corrections, the discrepancy factor among symmetry-related reflections (Laue class *mmm*) was R_{int} = 0.0554 and reflection conditions were consistent with the space group $Ccm2_1$, [13]. The anisotropic structural refinement was then performed using the SHELX-97 software [33], starting from the structure model of Evans [13]. The refined Flack parameter [33] was 0 within 1σ(*x*). Neutral atomic scattering factors of Ca, Si, V and O were used, according to the *International Tables for Crystallography* [34]. Convergence was achieved after a few refinement cycles. At the end of the refinement, no peak larger than +1.0/-0.8 $e^-/Å^3$ was present in the final difference-Fourier synthesis and the variance-covariance matrix showed no significant correlation between refined parameters.

An ETH-type DAC [28] was used to perform the *in situ* high-pressure experiment. 250 μm thick T301 steel foil was used as gasket, which was pre-indented to a thickness of about 140(5) μm before drilling a 300 μm hole by spark-erosion. The crystal of pentagonite, already used for the experiment at room conditions, was placed into the gasket hole together with few ruby micro-spheres to measure *P* by the ruby-fluorescence method [30]. A methanol:ethanol:water = 16:3:1 mixture was used as hydrostatic pressure-transmitting medium [10]. Lattice parameters were measured at 0.0001 GPa (crystal in DAC without any pressure medium, P_0), 0.36(5) (P_1), 0.64(5) (P_2), 1.51(5) (P_3), 1.70(5) (P_4), and 2.04(5) (P_5) GPa with a KUMA-KM4 diffractometer, equipped with a point-detector and a monochromatised Mo*K*α-radiation. Intensity data collections at 0.0001 GPa (crystal in DAC without any pressure medium, P_0), 1.51(5) (P_3), and 2.04(5) (P_5) GPa were performed on an Xcalibur-CCD diffractometer adopting the same experimental set-up and data collection protocol used with the crystal in air, but increasing the exposure time per frame to 20 s. At any given pressure, integrated intensity data were corrected

for Lp and absorption effects due to the crystal and the DAC using the ABSORB6.0 computer program [35]. No violation of reflection conditions compatible with space group $Ccm2_1$ was observed within the investigated *P*-range. At 2.5 GPa, a phase transition occurred, as shown by the aspect of the crystal observed with a polarizing microscope. Any attempt to index the diffraction data at $P > 2.5$ GPa was unsuccessful: the diffraction peaks showed significant broadening and did not allow to obtain reliable data. The optical inspection of the pressurized sample indicated inhomogeneities, the formation of domains, and optically-visible strains across the crystal. The *P*-induced crystal destruction was found to be irreversible.

The H*P*-structure refinements, based on the intensity data collected at 0.0001, 1.51(5) and 2.04(5) GPa, were conducted using soft geometrical restraints aimed to restrain Si-O and V-O distances to those obtained at room pressure (with the crystal in air), with an estimated standard deviation of ±0.01Å. This improved the stability of the H*P*-refinements, as soft restrains act as if they were additional experimental observations [33]. In order to reduce the number of refined variables, isotropic displacement parameters were refined by grouping all of the Si-sites and all of the O-sites.

RESULTS AND DISCUSSION

Details pertaining to the data collections and structure refinements for powder and single-crystal X-ray diffraction experiments are given in Table 1. The variation of the unit-cell parameters with *P* is reported in Tables 2 and 3. Hydrogen bond distances (Å) at different pressure conditions are in Table 4. Atomic coordinates and displacement parameters for the cavansite structure at P_{amb}, and in s.o. at 1.08(5), 3.27(5) and 6.45(5) GPa are given in Table S5

(supplementary materials). Selected interatomic distances (Å) and T-O-T angles (°) of cavansite at the various pressure points are listed in Table S6 (supplementary materials). Refined atomic positions and displacement parameters of pentagonite single-crystal in m.e.w. at the various pressure points are reported in Table S7 (supplementary materials). The corresponding bond distances and angles are listed in Table S8 (supplementary materials).

Elastic behavior and structural changes upon compression of cavansite

The evolution of the lattice parameters of cavansite with pressure is shown in Fig. 3. The elastic behavior is similar in the two media, thus we can exclude any PIH effect using the m.e.w. In order to describe the elastic behavior of this material, the unit-cell volume data for cavansite in m.e.w. and s.o. were fitted with different isothermal equations of state using the EOS-FIT6.0 program [36]. A second-order Birch-Murnaghan equation of state (BM-EoS) was adopted to describe the compressional behavior on the basis of the better standard deviation of the bulk modulus and a smaller $|P_{obs} - P_{calc}|_{max}$ value. The BM-EoS parameters, refined using the data obtained in m.e.w. and weighted by the uncertainties in P and V, are: V_0 = 1300(1) Å^3 and K_0 = 38.1(5) GPa. The calculation of bulk modulus in s.o. did not conform to a second-order BM-EoS model necessary for direct comparison with m.e.w. data. The cavansite bulk modulus is intermediate between the lowest (about 20 GPa) and the highest (about 65 GPa) [8-9] values determined for zeolites compressed in non-penetrating pressure transmitting media.

In both experiments, cavansite does not undergo complete amorphization and the original room pressure features are recovered upon decompression. No symmetry change is observed as a function of pressure.

Selected powder patterns of cavansite compressed in m.e.w. and s.o., respectively, are reported in Figures 1a and 1b. When the sample is compressed in m.e.w. from P_{amb} to 8.17(5)

GPa, a volume contraction of 14.3% is observed, while the unit-cell parameters **a**, **b** and **c** decrease by 2.8, 11.2 and 0.7%, respectively (Figure 3a). When the sample is compressed in s.o. from P_{amb} to 7.28(5) GPa, the volume contraction is 12.2%, while the unit cell parameters **a**, **b** and **c** decrease by 1.6, 10.3 and 0.3%, respectively (Figure 3b). The elastic behavior of cavansite is strongly anisotropic: the structure is almost uncompressible along [100] and [001], whereas it is highly compressible along [010]. Moreover, in m.e.w. a marked expansion of the **a** and **c** axes between 0.86(5) and 3.09(5) GPa is observed (Figure 3a). This effect is observed also in s.o. in the same pressure range but it is less pronounced.

As above reported, only the dataset of cavansite compressed in s.o. allowed a successful structure refinement. We are aware that the quality of the high pressure data can be influenced by several factors. In particular, the integrated intensities can be affected by poor statistics of the diffraction data and preferred orientations. For these reasons the high-pressure powder diffraction data are sometimes not sufficient to obtain robust structural information. Nevertheless, our structural refinements performed by the Rietveld methods appear to be reasonable considering that the weight of the applied soft-restraints was gradually decreased. Especially at high pressures, the Si-O distances and T-O-T angles (Table S6) are affected by rather high errors.

The room pressure data collected in the capillary and in the DAC confirmed the framework structure built by tetrahedral layers connected by vanadyl-type VO_5 square-based pyramids as reported by Evans [13] (Figure 5). The evaluation of the hydrogen-bond system is inferred by donor-acceptor (D…A) distances (Table 4) and is in agreement with the interactions described by Danisi et al. [20].

The structural evolution of cavansite at high pressure may be described in three main stages. At very low pressure (*i.e.*, ≤ 1.1 GPa), the tetrahedral framework shows significant distortion

(Figure 5). In particular, the Si1-O4-Si2 angle decreases from 128.4(5)° at P_{amb} to 117.2(15)° at 1.08 GPa, while Si1-O3-Si2 and Si1-O5-Si2 angles remain essentially unchanged (Table S6). The L/S ratio of the longest to the shortest cross sections of the eight-membered rings varies from 1.74 at P_{amb} to 1.63 at 1.08(5) GPa (Table S6). Concerning the hydrogen-bond system, the D…A distance of the O8…O3 interaction decreases from 3.564(2) to 3.32(4) Å (Table 4 and Figure 5). Thus, the compression of the pore system leads to strengthening of the hydrogen bonds between the extraframework H_2O molecules and the silicate sheet.

At intermediate pressure (1.1 GPa ≤ P ≤ 6 GPa), cavansite structure becomes strongly compressible along [010]. At the atomic scale, the O4-O4 distance between two tetrahedral layers decreases from 6.66 Å at P_{amb} to 5.61 Å at 3.27(4) GPa, leading to a severe compression of the porous system. Moreover, the L/S ratio of the longest to the shortest cross sections of the eight-membered rings varies from 1.74 at P_{amb} to 1.50 at 3.27 GPa (Table S6). Thus, the shape of the rings becomes more circular with increasing pressure.

At higher pressure (*i.e.*, > 6 GPa), the eight-membered rings in the **a**-**c** plane further reduce the L/S ratio to 1.25 and the **b** axis is further compressed. This leads to a O4-O4 distance between two adjacent tetrahedral layers of 4.96 Å. Moreover, the Si1-O5-Si2 angle decreases from 126.9(4)° at P_{amb} to 110.1(21)° at 6.45(5) GPa, while Si1-O3-Si2 and Si1-O4-Si2 angles strongly increased (Table S6). Interestingly, the pressure-induced deformation mechanism on the eight-membered rings described here is similar to that found in the K-GaSi-GIS structure [37]. The framework structure seems to respond to the effect of pressure reducing the ellipticity of the channels. Therefore, the shape of the rings tends to become more circular and regular. In case of K-GaSi-GIS, the L/S ratio decreases below a value of 1.60 near 1.60 GPa [37], while for cavansite the rounding effect of the ring is even more pronounced.

Pressure-induced over-hydration in pentagonite

As evident from Figure 4 and Table 3a, pentagonite in m.e.w. is almost incompressible. From the comparison between the volume evolutions in m.e.w. and s.o., it is clear that this behavior can be ascribed to the penetration of extra H_2O molecules, from the *P*-transmitting fluid, through the zeolitic channels. The new H_2O molecules made the channels more efficiently stuffed, and so less compressible. The pressure-induced over-hydration effect was observed first in the zeolite 4A [38] and in the natrolite family [39]. The authors observed a positive volume discontinuity suggesting the possible penetration of extra H_2O molecules into the cavities. Zeolites can undergo pressure-induced over-hydration following different effects: PIH based on increasing occupancy of already existing H_2O sites or PIH accompanied by the onset of new H_2O sites [40-41].

In order to demonstrate the pressure-induced over-hydration in pentagonite by locating the additional H_2O sites, the described *in situ* single-crystal X-ray experiment at high pressure was performed. The normalized volume values obtained from powder and single-crystal diffraction data plotted against the pressure show similar compressional patterns (Figure 4). As already reported by Evans [13], the distance between the Ca site and the oxygen of the H_2O molecule O9 is approximately 3.5 Å at room conditions. On this basis, the O9 molecule was not considered in the coordination environment of the Ca site but rather H-bonded to other H_2O molecules or framework oxygen atoms [13]. The structure refinement of Evans [13] showed that the equivalent displacement parameter of the O9 site is about 3-4 times that of the other H_2O molecules and more than 10 times those of the framework oxygen atoms. Our structure refinements at room conditions (with the crystal in air or in the DAC) confirm the previous experimental findings. At 1.51 GPa, a new H_2O molecule site was localized, leading to 5 H_2O molecules per formula unit. The Ca coordination changes from seven- to eight-fold (Table S8).

The new H_2O molecule (labelled as O10) leads to a rearrangement of the extraframework population, without significant distortion effects on the framework (Figure 6). In particular, O9 moves away from Ca. The Ca-O9 distance increases from 3.55 Å at P_{amb} to 4.62 Å at 2.04 GPa. On the contrary, the distance between the O8-O9 sites decreases from 2.94 Å at P_{amb} to 2.48 Å at 2.04 GPa. The O9 and O10 sites are rather close to each other at 2.04 GPa (nominally 2.1 Å), and are both affected by high displacement parameters (Table S7c). A careful inspection of the difference-Fourier map of the electron density shows evidence of positional disorder around the O9 site, which reflects its high displacement factor. The refined O9-O10 distance is drastically affected by the positional disorder of O9. The O9-O10 distance obtained by the structure refinement was then corrected for "non-correlation motion" following the protocol of Busing and Levy [42]. The corrected distance is 2.30 Å. In addition, the estimated "upper bound", following Busing and Levy [42], is 2.45 Å. We can then reasonably consider that the actual distance between the O9 and O10 molecules ranges between 2.3 and 2.5 A, ascribable to an H-bond interaction in a compressed configuration. Above 2.5 GPa, it was not possible to collect single-crystal data because of the high mosaicity of the crystal in response to a *P*-induced phase transition.

Structural changes upon compression of pentagonite

In Figures 2a and 2b, selected powder patterns of pentagonite compressed in m.e.w. and s.o. are reported, respectively. The onset of new peaks (indicated with red boxes) in m.e.w. suggested a *P*-induced symmetry change. The Le Bail fit of the powder-pattern profile indicates a phase transition from an orthorhombic to a triclinic cell (Table 3a). The orthorhombic to triclinic phase transition occurs between 2.45(5) and 2.96(5) GPa and is reversible (Table 3a). In Figure 7a, the phase transition is characterized by 1.4% shortening of the **b** axis (interlayer separation) and

increase of **a** and **c** by 0.86 and 0.74 %, respectively, coupled with a significant distortion of the unit cell (Table 3a). As we could not refine the triclinic structure, the observed cell modifications could not be structurally interpreted.

During the s.o. experiment (Table 3b and Figure S8), at 1.71(5) GPa, the diffraction pattern changed significantly. In particular, the reflection initially indexed as 040 splits, suggesting also in this case a *P*-induced transformation to a triclinic phase.

As already observed for cavansite under high-pressure, the main structural deformation of pentagonite in both media occurs along **b**. Nevertheless, in pentagonite, the **b** axis did not undergo a drastic change comparable to that of cavansite. Specifically, in m.e.w., pentagonite **b** axis decreased only by 3.6% (Figure 7) compared to 11.2% in cavansite m.e.w. The overall compressibility of pentagonite in s.o., characterized by a volume contraction of 11.6%, is comparable to that of cavansite in s.o. with volume decrease by 12.2%.

The evolution of the volume compressibility of pentagonite in s.o. was described using a second order BM-EoS. To take into account the occurrence of the phase transition, data were divided into two data sets above and below 2.0 GPa, respectively. In s.o. the bulk-modulus is K_0 = 38(3) GPa and K_0 = 49(2), below and above the phase-transition pressure, respectively. This indicates a decreased compressibility above 2.0 GPa. The bulk modulus of pentagonite compressed in s.o. below the phase transition is comparable to that of cavansite (K_0 = 38.1(5) GPa).

In pentagonite compressed in m.e.w., a pressure-induced phase transition to a triclinic phase is observed at about 2.5 GPa in both single-crystal and powder diffraction experiments in m.e.w. Thus, the total surface area (powder vs. single-crystal) seems not to be a crucial factor to promote pressure-induced modifications in this microporous material. Otherwise, the nature of the pressure-transmitting medium appears to influence the onset of the phase transition and also

the degree of triclinic distortion in powder experiments. In fact, the penetration of extra H_2O molecules, from the *P*-transmitting fluid, defers the occurrence of the pressure-induced phase transition compared to non-penetrating media.

CONCLUDING REMARKS

Unexpectedly, only pentagonite, but not cavansite, compressed in m.e.w. showed PIH. In this different response to pressure, the role of the Ca-coordination could be crucial. In cavansite, Ca is eight-fold coordinated while in pentagonite it is only seven-fold. This makes pentagonite more suitable to accept an additional H_2O molecule. The polymorphic structures of cavansite and pentagonite belong formally to the same group of "phyllosilicates" and are thus strongly related. At room conditions, the density of cavansite (V = 1288.9 Å^3) is slightly higher than the one of pentagonite (V = 1309.5 Å^3). Under ambient conditions, the "tetrahedral sheet" composed of six-membered rings in pentagonite is more densely packed (**a** · **c** = 93.1 Å^2), than the one in cavansite (**a** · **c** = 94.3 Å^2) composed of four- and eight-membered rings. However, the interlayer separation in pentagonite (**b**/2 = 7.034 Å) is significantly wider than in cavansite (**b**/2 = 6.683 Å), which is responsible for the difference in density. All H_2O molecules in pentagonite and cavansite occupy the interlayer space. In this light, one could argue that pentagonite is more favorable accepting an additional H_2O molecule under high-pressure conditions (PIH).

At 2.04 GPa in the overhydrated phase (m.e.w. pressure medium), the tetrahedral sheet of pentagonite preserves essentially the same extension of 93.0 Å^2, with an interlayer separation of **b**/2 = 7.00 Å. Compression of pentagonite in s.o. (no PIH) at a comparable pressure (2.15 GPa) maintains the "interlayer distance" to **b**/2 = 7.00 Å but reduces the expansion of the tetrahedral sheet to 90.0 Å^2. The different anisotropic compression in pentagonite when compressed in m.e.w. or s.o. may be explained by the formation of a "puckered sheet" of tetrahedra in s.o.

whereas in m.e.w. the sheet remains stretched (also confirmed by the single-crystal structure refinement in m.e.w.). Probably the space filling due to penetration of the additional H_2O molecule in m.e.w. hinders the formation of a puckered sheet.

The effect on the material elastic response of the unusual presence of vanadyl-type square based pyramids in the framework has no record in the literature. To highlight the role of VO_5 on framework distortion and contraction, we compare the response to compression of the zeolite gismondine to that of cavansite. In response to a pressure of 7.4(5) GPa, the cell volume decrease of gismondine in s.o. [43] is approximately 8% with shortening a of the **a** and **c** parameters (perpendicular to the 8- and 4-rings layers corresponding to the cavansite tetrahedral sheets) by 4 and 3%, respectively. Cavansite in s.o. shows a volume contraction by 12.2%, accompanied with a decrease by 10% of **b** parameter, perpendicular to the tetrahedral sheets. The fact that cavansite is more compressible than gismondine is related to the presence of VO_5 pyramids connecting the tetrahedral layers along [010]. The V-O-T angles (Table S6) increase from P_{amb} to 6.45(5) GPa in order to accommodate the effect of the pressure on the framework. Moreover, the T-O-T angles in cavansite mutually distort in an opposite sense (*antirotate,* [44]) while the V-O-T angles vary in the same sense (*corotate,* [44]) when the volume decreases (Table S6). The same behavior is observed in cavansite under high-temperature conditions [20], indicating a common deformation mechanism of the framework upon dehydration and high-pressure conditions.

Acknowledgment

Discussions with Martin Kunz (Lawrence Berkeley National Laboratory), Martin Fisch and Frank Gfeller (University of Bern) on interpreting DAC powder synchrotron data are highly appreciated. This work was supported by the Italian MIUR, within the framework of the project PRIN2010-11 “Dalle materie prime del sistema Terra alle applicazioni tecnologiche: studi cristallochimici e strutturali”.

Appendix A. Supplementary data

Supplementary data associated with the article can be found, in the online version, at http.....

REFERENCES

[1] S. Krivovichev, in: G. Ferraris, S. Merlino (Eds.), Micro- and mesoposorous mineral phases. Reviews in Mineralogy and Geochemistry, vol. 57, Washington, USA, 2005, pp. 17-68.

[2] X. Wang, L. Lumei, A.J. Jacobson, Angew. Chem. Int. Ed. 40 (2001) 2174.

[3] X. Wang, L. Lumei, A.J. Jacobson, J. Am. Chem. Soc. 124 (2002) 7812.

[4] J.Huang, X. Wang, L. Lumei, A.J. Jacobson, Solid St. Sci. 4 (2002) 1193.

[5] S.J. Datta, K.B. Yoon, Top. Catal. 53 (2010) 1311.

[6] S.J. Datta, K.B. Yoon, Micropor. Mesopor. Mater. 143 (2011) 115.

[7] H. Kimizuka, S.Ogata, J. Li, Y. Shibutani, Physic. Rev. B 75 (2007) 054109/1.

[8] G.D. Gatta, Z. Krist. 223 (2008) 160.

[9] G.D. Gatta, Y. Lee, Mineral. Mag. 78 (2014) 267.

[10] R.J. Angel, M. Bujak, J. Zhao, G.D. Gatta, S.D. Jacobsen, J. Appl. Crystallogr. 40 (2007) 26.

[11] S. Klotz, J-C. Chervin, P. Munsch, G. Le Marchand, J. Phys. D: Appl. Phys., 42 (2009) 075413/1.

[12] L. Leardini, S. Quartieri, A. Martucci, G. Vezzalini, V. Dmitriev, Z. Krist. 227 (2012) 514.

[13] H.T.Jr. Evans, Am. Mineral. 58 (1973) 412.

[14] K.F. Fischer, Am. Mineral. 48 (1963) 664.

[15] R. Rinaldi, J.J. Pluth, J.V. Smith, Acta Crystallogr. B31 (1975) 1598.

[16] A.V. Phadke, A. Apte, Mineral. Mag. 58 (1994) 501.

[17] K.B. Powar, K. Byrappa, J. Mineral. Petrol. Sci. 96 (2001) 1.

[18] P.S.R. Prasad, S.K. Prasad, Mater. Chem. Phys. 105 (2007) 395.

[19] N. Ishida, M. Kimata, N. Nishida, T. Hatta, M. Shimizu, T. Akasaka, J. Mineral. Petrol. Sci. 104 (2009) 241.

[20] R.M. Danisi, T. Armbruster, B. Lazic, Am. Mineral. 97 (2012) 1874.

[21] R.M. Danisi, T. Armbruster, B. Lazic, J. Solid St. Chem. 197 (2013) 508.

[22] A. Martucci, G. Cruciani, Dehydration dynamics of cavansite probed by in situ synchrotron powder diffraction. V International Workshop on Oxide Based Materials (Oxide 2012) & AIZ Days 2012. Torino, 23-27/9/2012.

[23] T.R. Ravindran, A.K. Arora, G. Parthasarathy, J. Phys.: Conf. Ser., 377 (2012) 012004/1.

[24] A.P. Hammersley, S.O. Svensson, M. Hanfland, A.N. Fitch, D. Hausermann, High Pressure Res. 14 (1996) 235.

[25] A.C. Larson, R.B. Von Dreele, General Structure Analysis System (GSAS), Report LAUR 86-748, Los Alamos National Laboratory, Los Alamos, New Mexico, 2000.

[26] B.H. Toby, J. Appl. Crystallogr. 34 (2001) 210.

[27] P. Thomson, D.E. Cox, J.B. Hastings, J. Appl. Crystallogr. 20 (1987) 79.

[28] R. Miletich, D.R. Allan, W.F. Kush, in: R.M. Hazen, R.T. Downs (Eds.), High-temperature and high-pressure crystal chemistry, Reviews in Mineralogy and Geochemistry, vol. 41, Mineralogical Society of America, Washington, D.C., USA; 2000, pp. 445-519.

[29] R.A. Forman, G.J. Piermarini, J.D. Barnett, S. Block, Science 176 (1972) 284.

[30] H.K. Mao, J. Xu, P.M. Bell, J. Geophys. Res. 91 (1986) 4673.

[31] A. Le Bail, H. Duroy, J.L. Fourquet, Math. Res. Bull. 23 (1988) 447.

[32] Agilent, Xcalibur CCD system, CrysAlis Software system, 2012.

[33] G.M. Sheldrick, Acta Crystallogr. A64 (2008) 112.

[34] A.J.C. Wilson, E. Prince (Eds.), International Tables for X-ray Crystallography, Volume C: Mathematical, physical and chemical tables (2nd Edition), Kluwer Academic, Dordrecht, NL, 1999.

[35] R. J. Angel, J. Appl. Crystallogr. 37 (2002) 486.

[36] R.J. Angel, EOS-FIT V6.0 Computer Program. Crystallography Laboratory, Department of Geological Science, Virginia Tech, Blacksburg, USA, 2001.

[37] Y. Lee, S.J. Kim, C.C. Kao, T. Vogt, J. Am. Chem. Soc. 130 (2008) 2842.

[38] R.M. Hazen, L.W. Finger, J. Appl. Phys. 56 (1984) 1838.

[39] Y. Lee, T. Vogt, J.A. Hriljac, J.B. Parise, G. Artioli, J. Am. Chem. Soc. 124 (2002) 5466.

[40] S. Ori, S. Quartieri, G. Vezzalini, V. Dimitriev, Am. Mineral. 93 (2008) 1393.

[41] G. Vezzalini, R. Arletti, S. Quartieri, Acta Crystallogr. B70 (2014) 444.

[42] W.R. Busing, H.A. Levy, Acta Crystallogr. 17 (1964) 142.

[43] C. Betti, E. Fois, E. Mazzucato, C. Medici, S. Quartieri, G. Tabacchi, G. Vezzalini, V. Dmitriev, Micropor. Mesopor. Mater. 103 (2007) 190.

[44] W.H. Baur, J. Solid State Chem. 97 (1992) 243.

FIGURES

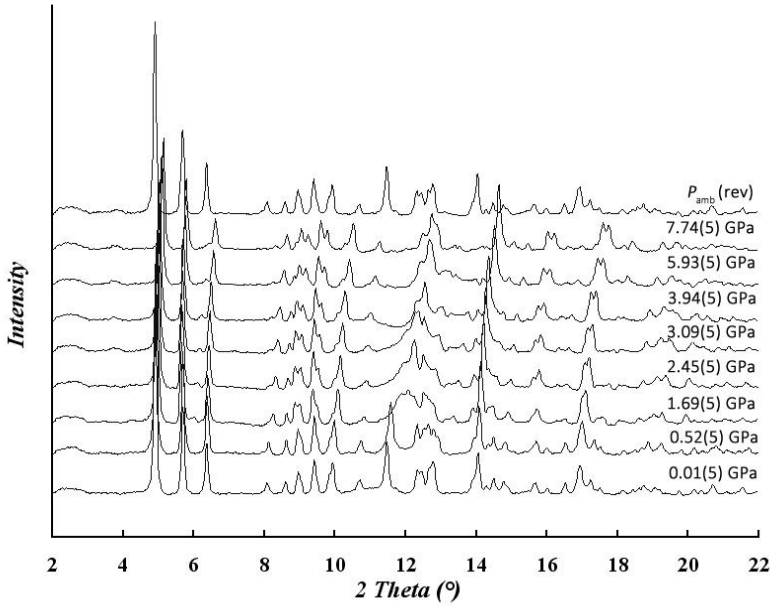

Figure 1a: Selected integrated powder patterns with background subtracted of cavansite in m.e.w.

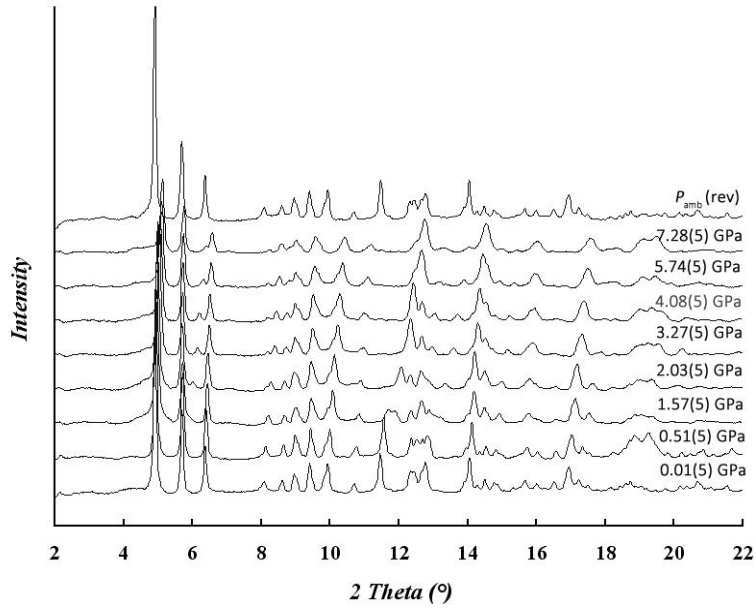

Figure 1b: Selected integrated powder patterns with background subtracted of cavansite in s.o.

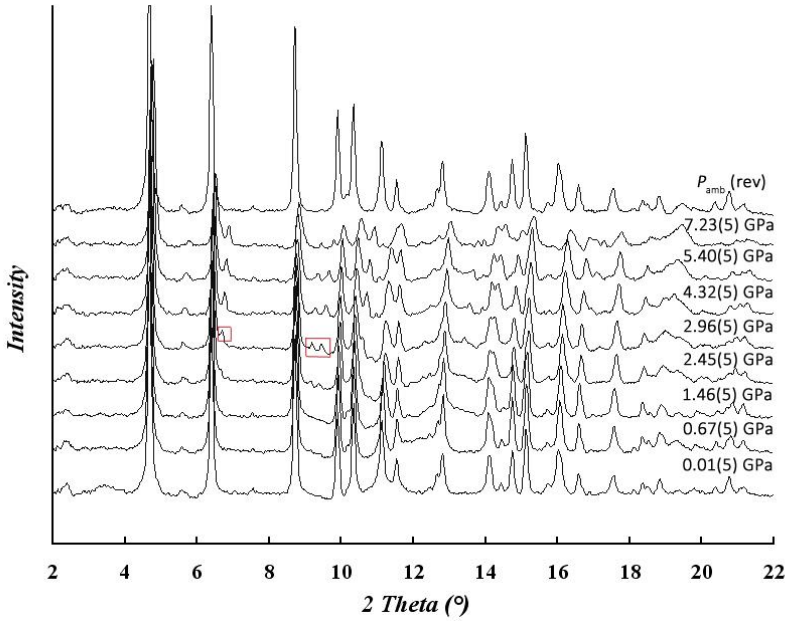

Figure 2a: Selected integrated powder patterns with background subtracted of pentagonite in m.e.w. The red boxes highlight changes in the diffraction pattern.

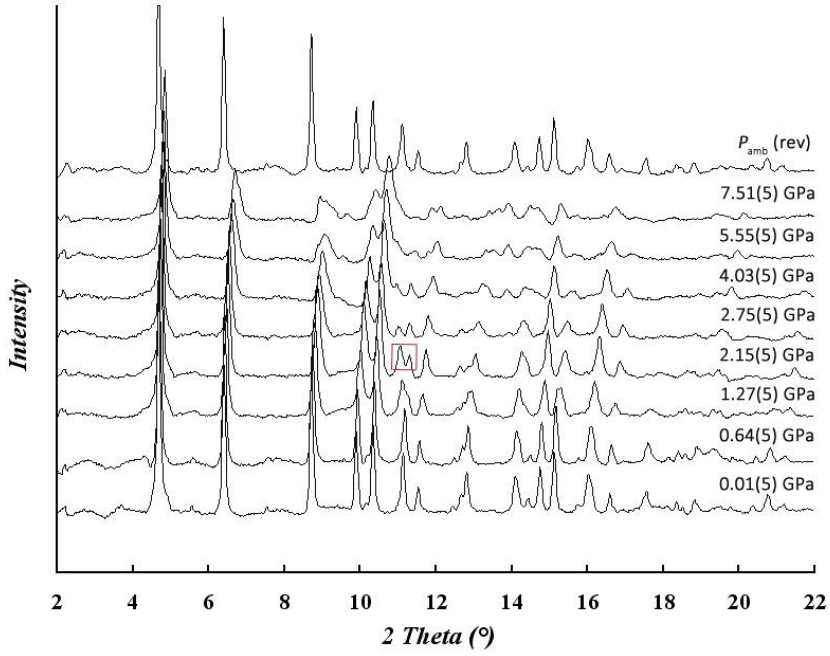

Figure 2b: Selected integrated powder patterns with background subtracted of pentagonite in s.o. The red boxes highlight changes in the diffraction pattern.

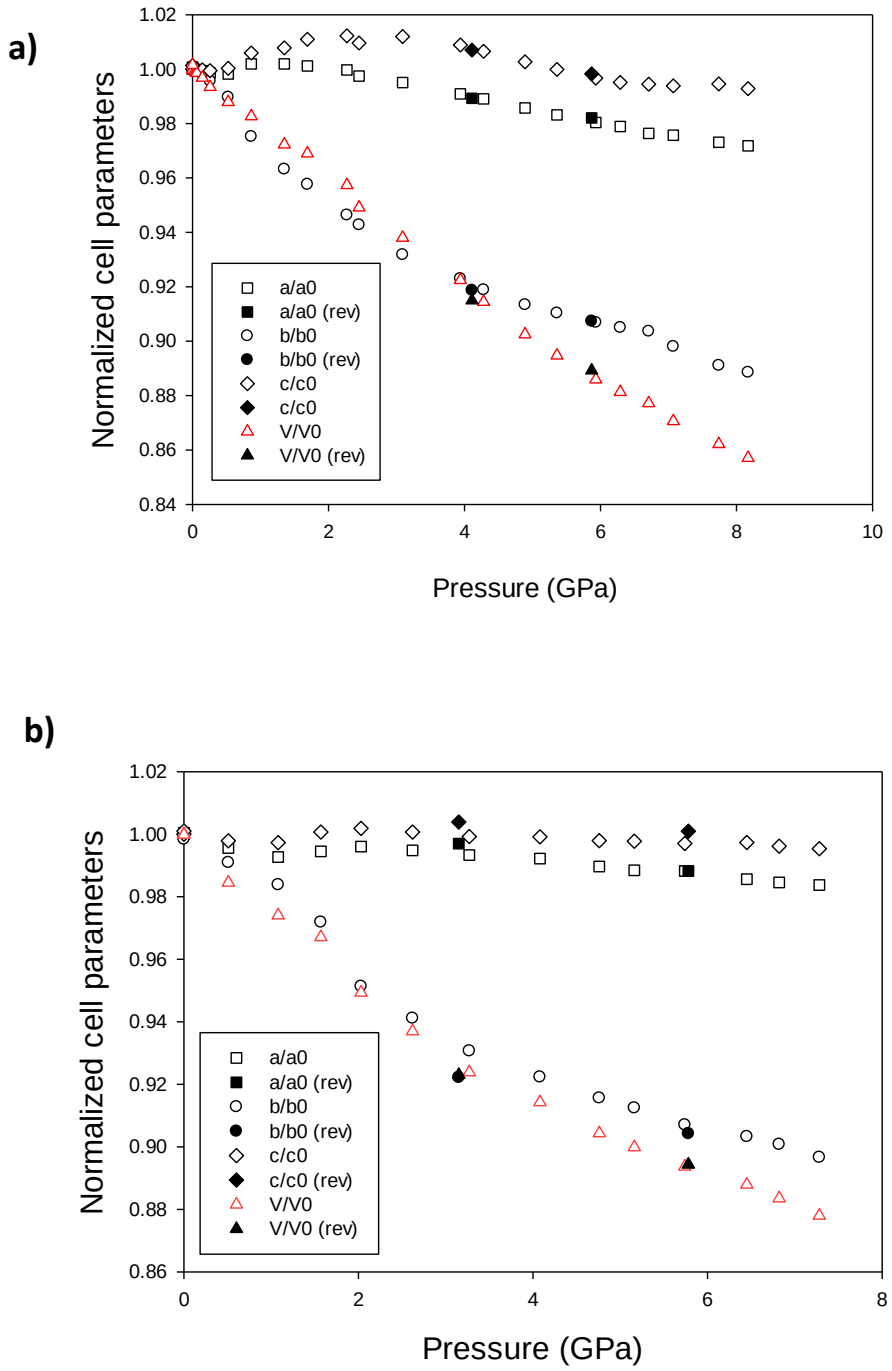

Figure 3: Variation of cavansite lattice parameters *vs.* pressure: a) compressed in m.e.w. and b) in s.o. The size of the symbols is larger than the associated e.s.d. values.

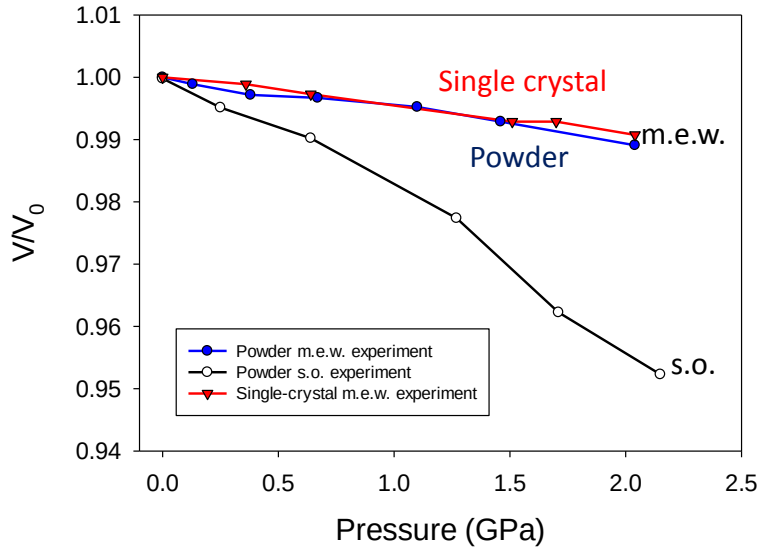

Figure 4: Evolution of the normalized unit-cell volume (V/V_0) of pentagonite with P, in m.e.w. (powder and single-crystal data) and s.o. (powder data).

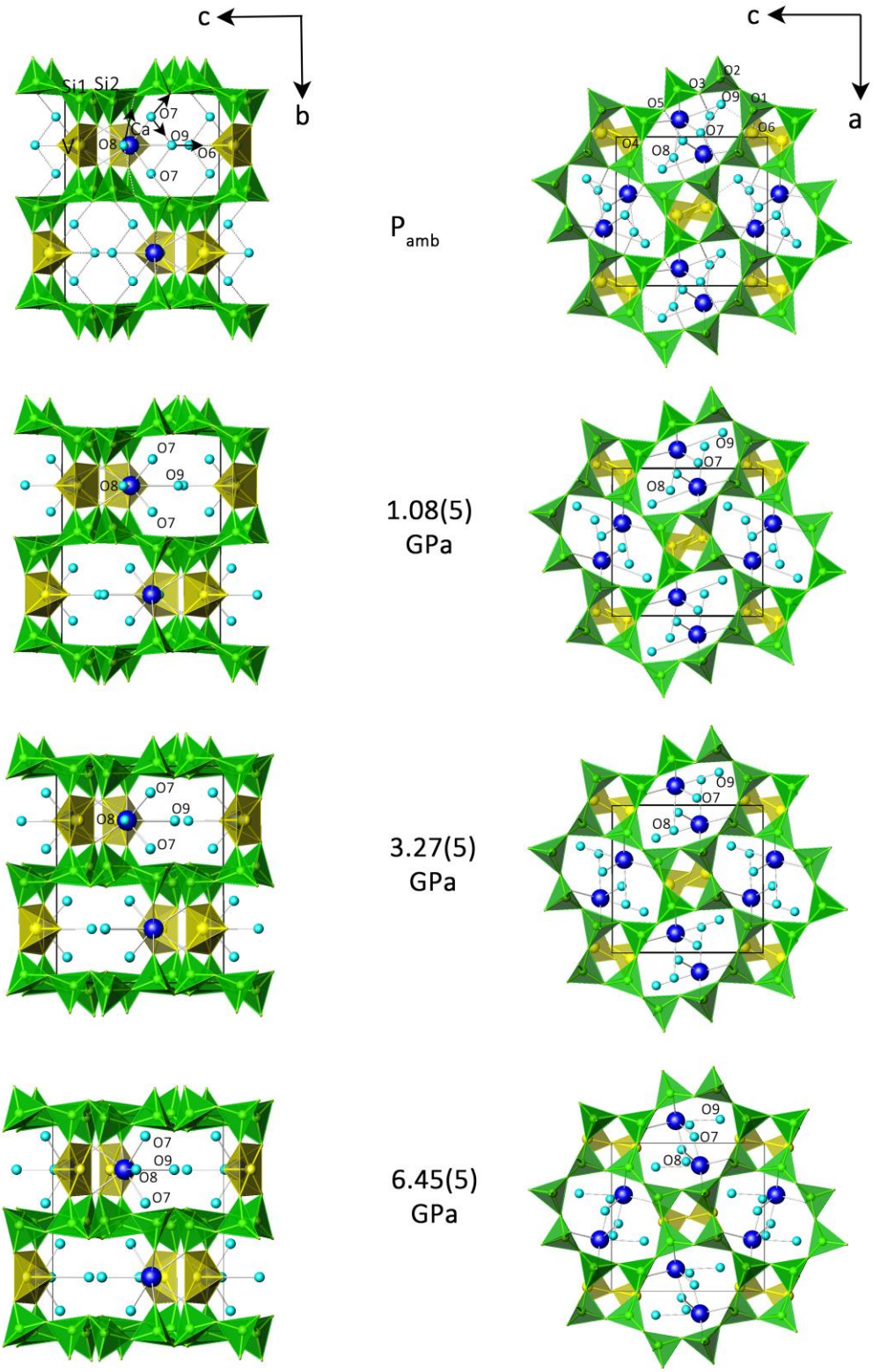

Figure 5: Framework of cavansite at P_{amb} and high-pressure conditions. On the left: projection along **a**. On the right: projection along **b**. The green polyhedra represent Si tetrahedra, while the yellow polyhedra are the VO_5 square-based pyramids. Calcium is in blue and oxygen atoms at H_2O sites are shown as light blue spheres. Hydrogen-bond acceptor interactions are shown by gray dashed connectors. The black arrows (upper left drawing) indicate the direction to the acceptor. The H_2O molecules O7, O8, and O9 are labeled.

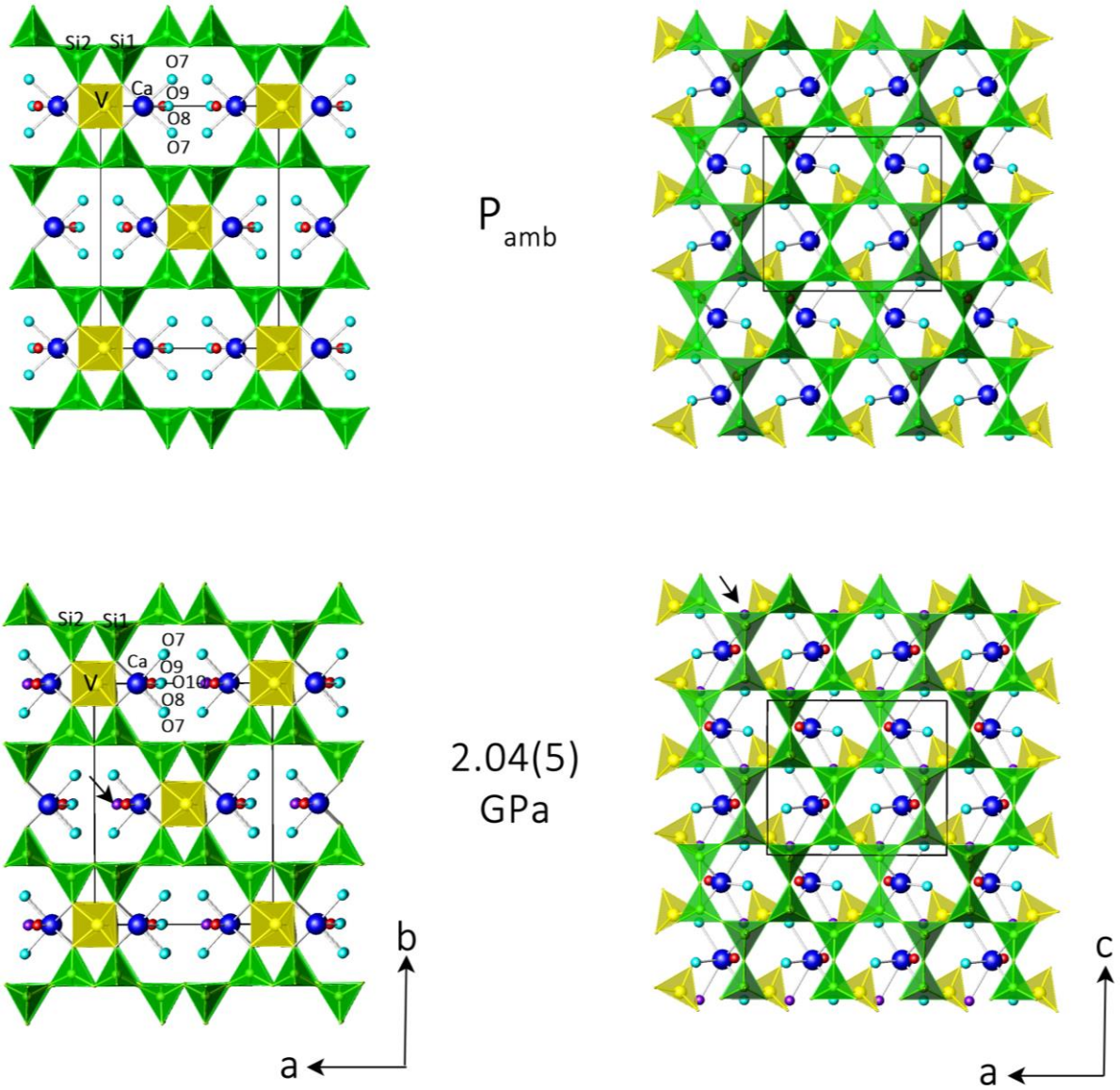

Figure 6: Framework of pentagonite at P_{amb} and 2.04(5) GPa. On the left: projection along **c**. On the right: projection along **b**. The green polyhedra represent Si tetrahedra, while the yellow polyhedra are the VO_5 square-based pyramids. Calcium is in blue and oxygen atoms at H_2O sites are shown as light blue spheres. The H_2O molecule O9 is shown in red, while the new H_2O molecule O10 is in violet and indicated by an arrow.

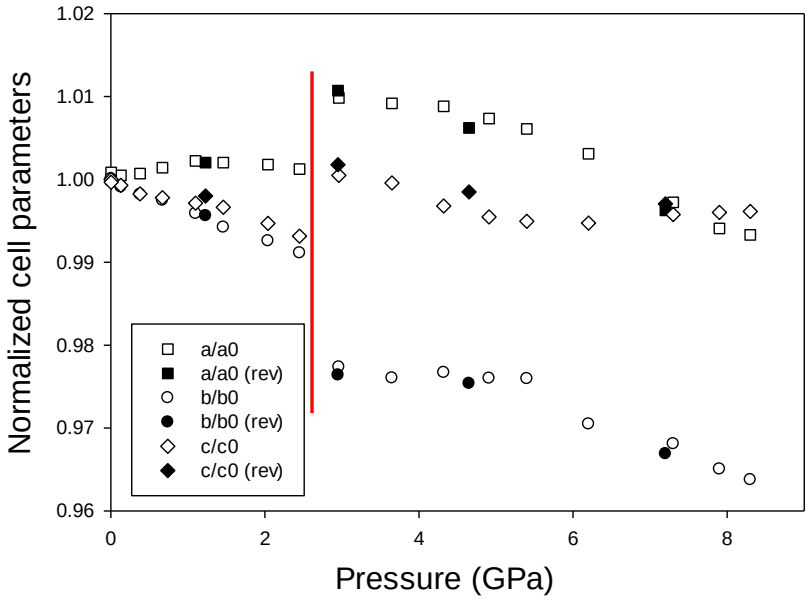

Figure 7a: Variation of pentagonite lattice parameters vs. pressure compressed in m.e.w. The size of the symbols is larger than the associated e.s.d. values. The red line indicates the phase transition orthorhombic to triclinic between 2.45(5) and 2.96(5) GPa.

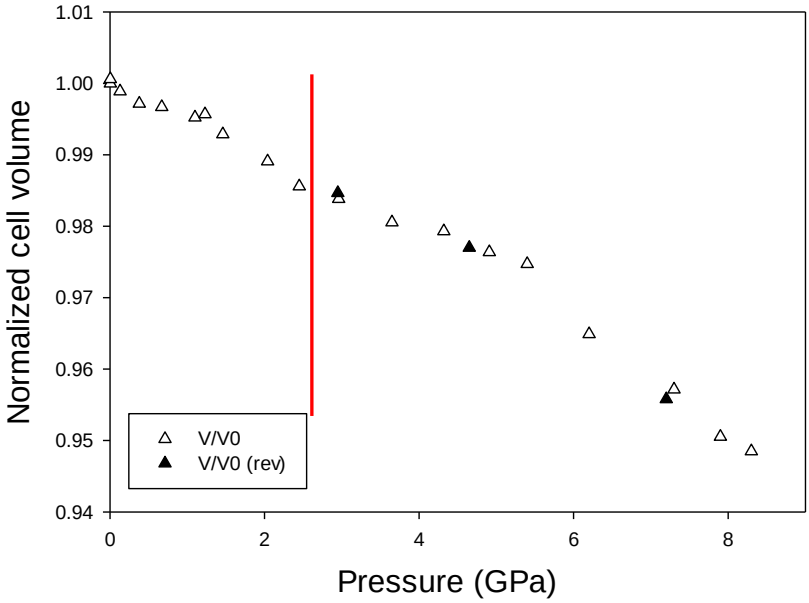

Figure 7b: Variation of pentagonite cell volume vs. pressure compressed in m.e.w. The size of the symbols is larger than the associated e.s.d. values. The red line indicates the phase transition orthorhombic to triclinic between 2.45(5) and 2.96(5) GPa.

SUPPLEMENTARY MATERIAL: FIGURE S8

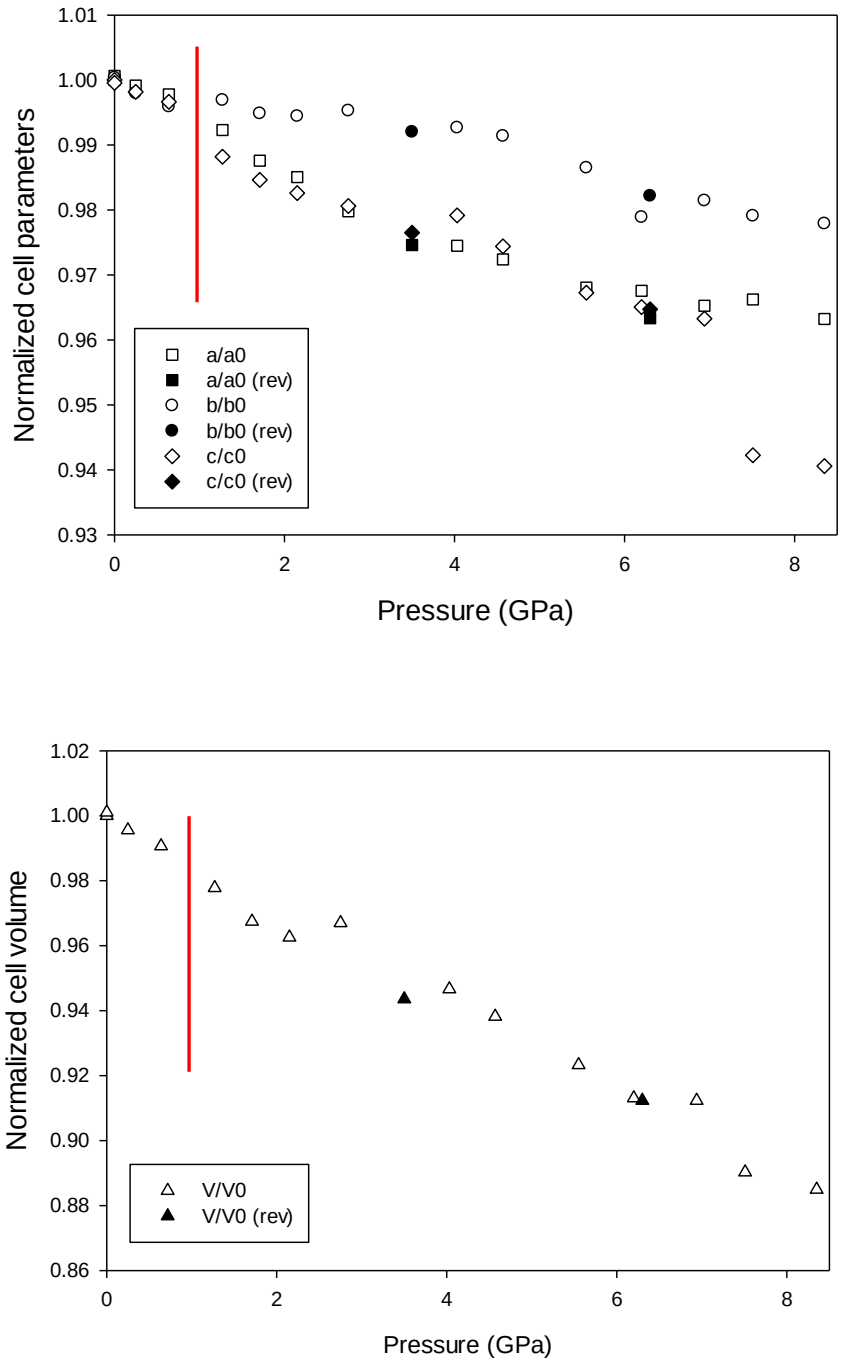

Figure S8: Variation of pentagonite lattice parameters vs. pressure compressed in s.o. The size of the symbols is larger than the associated e.s.d. values. The red line indicates the phase transition orthorhombic to triclinic between 1.27(5) and 1.71(5) GPa. Original data are summarized in Table 3b.

TABLES

TABLE 1A: PARAMETERS FOR X-RAY POWDER DATA COLLECTION AND CRYSTAL-STRUCTURE REFINEMENT OF CAVANSITE IN S.O.

Crystal data	P_{amb} capillary	1.08(3) GPa	3.27(4) GPa	6.45(5)GPa
Unit cell dimensions (Å)	*a* = 9.64247 (21) *b* = 13.66975 (29) *c* = 9.80094 (25)	*a* = 9.5844(9) *b* = 13.4707(13) *c* = 9.7860 (14)	*a* = 9.5944(16) *b* = 12.7406(22) *c* = 9.8097(26)	*a* = 9.5240(22) *b* = 12.3657(30) *c* = 9.771(4)
Volume ($Å^3$)	1291.86 (5)	1263.46 (24)	1199.1(4)	1150.7(6)
Space group	*Pnma* (No. 62)	*Pnma* (No. 62)	*Pnma* (No. 62)	*Pnma* (No. 62)
Z	4	4	4	4
Chemical formula	$Ca(VO)(Si_4O_{10})•4H_2O$	$Ca(VO)(Si_4O_{10})•4H_2O$	$Ca(VO)(Si_4O_{10})•4H_2O$	$Ca(VO)(Si_4O_{10})•4H_2O$
Detector	PILATUS	PILATUS	PILATUS	PILATUS
X-ray radiation	λ = 0.682534 Å	λ = 0.682534 Å	λ = 0.682534 Å	λ = 0.682534 Å
No. of observations	2127	1498	1498	1485
No. of reflections	1022	432	526	506
Refinement of the structure				
No. of variables	61	67	65	64
xR_p (%)	1.94	*	*	*
R_{wp} (%)	2.58	*	*	*
R F**2(%)	6.59	11.34	7.53	14.27

***** The values for xR_p and R_{wp} are physically not meaningful (<1) because they originate from refinements including the background.

TABLE 1B: PARAMETERS FOR X-RAY SINGLE-CRYSTAL DATA COLLECTION AND CRYSTAL-STRUCTURE REFINEMENT OF PENTAGONITE IN M.E.W.

Crystal data	P_{amb} air	1.51(5)GPa	2.04(5) GPa
Unit cell dimensions (Å)	a = 10.335(2)	a = 10.382(2)	a = 10.392(3)
	b = 14.025(2)	b = 14.024(9)	b = 14.027(11)
	c = 8.9711(10)	c = 8.934(2)	c = 8.910(2)
Volume (Å^3)	1300.3(3)	1300.8(9)	1298.8(11)
Space group	$Ccm2_1$ (No. 36)	$Ccm2_1$ (No. 36)	$Ccm2_1$ (No. 36)
Z	4	4	4
Chemical formula	$Ca(VO)(Si_4O_{10})\bullet 4H_2O$	$Ca(VO)(Si_4O_{10})\bullet 5H_2O$	$Ca(VO)(Si_4O_{10})\bullet 5H_2O$
Crystal size (mm)	170 x 140 x 60µm^3	170 x 140 x 60µm^3	170 x 140 x 60µm^3
Diffractometer	Xcalibur CCD	Xcalibur CCD	Xcalibur CCD
X-ray radiation	Mo$K\alpha$ λ = 0.71071 Å	Mo$K\alpha$ λ = 0.71071 Å	Mo$K\alpha$ λ = 0.71071 Å
Scan type	ω	ω	ω
Scan width (°/frame)	1	1	1
Exposure (s/frame)	10	20	20
Index ranges	$-14 \le h \le 16$	$-17 \le h \le 17$	$-17 \le h \le 17$
	$-22 \le k \le 18$	$-5 \le k \le 5$	$-5 \le h \le 5$
	$-12 \le l \le 11$	$-15 \le l \le 15$	$-15 \le h \le 15$
Max θ	34.91	39.03	39.08
No. of measured reflections	11298	3043	2915
No. of unique reflections	1972	903	881
No. of unique reflections with F_o>4σ(F_o)	1522	445	468
Refinement of the structure			
No. of parameters used in refinement	105+1 restraint	46+10 restraints	46+10 restraints
R_{int}	0.0554	0.1215	0.0953
R_σ	0.0810	0.1880	0.1533
$R1$, $I > 2\sigma(I)$	0.0432	0.0729	0.0838
$R1$, all data	0.0719	0.1542	0.1472
w$R2$ (on F^2)	0.0551	0.0884	0.0895
GooF	1.343	1.463	1.561
$\Delta\rho_{min}$ (-e / Å^3)	-0.75 close to V	-0.59 close to O8	-0.62 close to V
$\Delta\rho_{max}$ (e / Å^3)	1.03 close to V	0.65 close to O9	0.89 close to O6

TABLE 2A: UNIT-CELL PARAMETERS OF CAVANSITE AS A FUNCTION OF *P* (POWDER COMPRESSED IN M.E.W.). REV= PATTERNS COLLECTED UPON *P* RELEASE.

Cavansite (m.e.w.)				
P (GPa)	*a* (Å)	*b* (Å)	*c* (Å)	*V* (Å^3)
P_{amb}	9.6622(7)	13.6819(10)	9.8116(11)	1297.06(19)
0.03(5)	9.6611(6)	13.6786(9)	9.8127(10)	1296.74(18)
0.04(5)	9.6593(6)	13.6744(9)	9.8114(10)	1295.94(17)
0.07(5)	9.6602(6)	13.6706(9)	9.8118(10)	1295.76(17)
0.14(5)	9.6570(7)	13.6543(10)	9.8099(11)	1293.5(2)
0.26(5)	9.6490(8)	13.6226(11)	9.8071(12)	1289.1(2)
0.52(5)	9.6452(9)	13.5408(13)	9.8154(14)	1281.9(3)
0.86(5)	9.6829(14)	13.349(2)	9.870(2)	1275.8(4)
1.35(5)	9.6817(15)	13.177(2)	9.890(3)	1261.7(4)
1.69(5)	9.6740(16)	13.102(3)	9.920(3)	1257.4(5)
2.45(5)	9.6381(16)	12.899(3)	9.907(3)	1231.6(5)
3.09(5)	9.6147(16)	12.757(3)	9.929(3)	1217.8(5)
3.94(5)	9.5747(14)	12.628(3)	9.900(2)	1197.0(4)
4.28(5)	9.5563(18)	12.573(3)	9.877(3)	1186.7(5)
4.89(5)	9.5245(16)	12.497(3)	9.839(2)	1171.1(4)
5.36(5)	9.5002(15)	12.456(3)	9.811(2)	1161.0(4)
5.93(5)	9.4732(16)	12.408(3)	9.780(2)	1149.6(4)
6.29(5)	9.4587(17)	12.382(3)	9.765(2)	1143.6(4)
6.71(5)	9.4345(9)	12.364(2)	9.7583(9)	1138.3(3)
7.07(5)	9.4280(13)	12.287(3)	9.7521(12)	1129.7(3)
7.74(5)	9.4028(7)	12.1918(13)	9.7589(8)	1118.74(17)
8.17(5)	9.3901(7)	12.1571(12)	9.7422(8)	1112.14(17)
5.87(5) (rev)	9.4893(14)	12.414(4)	9.7954(16)	1153.9(4)
4.11(5) (rev)	9.5591(18)	12.570(3)	9.881(3)	1187.3(5)
2.27(5) (rev)	9.6597(15)	12.948(3)	9.933(2)	1242.3(4)
P_{amb} (rev)	9.6700(6)	13.6783(9)	9.8254(10)	1299.60(18)

TABLE 2B: UNIT-CELL PARAMETERS OF CAVANSITE AS A FUNCTION OF *P* (POWDER COMPRESSED IN S.O). REV= PATTERNS COLLECTED UPON *P* RELEASE.

Cavansite (s.o.)				
P (GPa)	*a* (Å)	*b* (Å)	*c* (Å)	*V* (Å^3)
P_{amb}	9.6569(13)	13.6912(19)	9.814(2)	1297.6(4)
0.51(5)	9.6144(15)	13.567(2)	9.794(2)	1277.5(4)
1.08(5)	9.5844(9)	13.4707(13)	9.7860(14)	1263.5(2)
1.57(5)	9.598(2)	13.352(4)	9.813(4)	1257.5(7)
2.03(5)	9.6187(16)	13.025(3)	9.833(3)	1231.9(5)
2.62(5)	9.6063(13)	12.886(2)	9.823(2)	1215.9(4)
3.27(5)	9.5944(16)	12.741(2)	9.810(3)	1199.1(4)
4.08(5)	9.5815(16)	12.628(2)	9.806(3)	1186.4(4)
4.76(5)	9.5572(14)	12.536(2)	9.796(2)	1173.6(4)
5.16(5)	9.5441(19)	12.493(3)	9.791(3)	1167.4(5)
5.74(5)	9.5413(16)	12.420(2)	9.784(3)	1159.4(4)
6.45(5)	9.524(2)	12.366(3)	9.771(4)	1150.7(6)
6.82(5)	9.510(2)	12.326(4)	9.785(4)	1147.0(6)
7.28(5)	9.498(2)	12.275(4)	9.778(4)	1140.0(6)
5.78(5) (rev)	9.541(2)	12.379(5)	9.825(4)	1160.5(7)
3.15(5) (rev)	9.6279(15)	12.626(2)	9.853(2)	1197.7(4)
P_{amb} (rev)	9.6614(11)	13.6697(17)	9.8242(18)	1297.5(3)

TABLE 3A: UNIT-CELL PARAMETERS OF PENTAGONITE AS A FUNCTION OF *P* (POWDER COMPRESSED IN M.E.W.). REV= PATTERNS COLLECTED UPON *P* RELEASE.

Pentagonite (m.e.w.)							
P (GPa)	*a* (Å)	*b* (Å)	*c* (Å)	α (°)	β (°)	γ (°)	*V* (Å^3)
P_{amb}	10.3830(13)	14.0977(13)	8.9897(7)				1315.9(2)
0.13(5)	10.3880(13)	14.0850(12)	8.9833(6)				1314.4(2)
0.38(5)	10.3903(15)	14.0723(15)	8.9740(8)				1312.2(3)
0.67(5)	10.3975(12)	14.0633(12)	8.9699(7)				1311.6(2)
1.10(5)	10.4046(12)	14.0425(12)	8.9616(7)				1309.4(2)
1.46(5)	10.4027(13)	14.0169(13)	8.9567(7)				1306.0(2)
2.04(5)	10.3985(15)	13.9917(16)	8.9404(8)				1300.8(3)
2.45(5)	10.3933(18)	13.9703(17)	8.9257(10)				1296.0(3)
2.96(5)	10.4850(11)	13.7786(17)	8.9940(7)	86.197(14)	86.902(11)	89.567(8)	1294.6(2)
3.65(5)	10.4783(14)	13.760(2)	8.9858(8)	86.069(11)	86.609(11)	89.989(10)	1290.3(3)
4.32(5)	10.4745(14)	13.7692(16)	8.9609(8)	86.672(13)	87.183(12)	89.392(10)	1288.6(3)
4.91(5)	10.4593(17)	13.760(3)	8.9490(12)	86.93(3)	87.49(2)	89.289(15)	1284.8(4)
5.40(5)	10.4463(18)	13.759(2)	8.9442(12)	86.878(18)	87.863(14)	89.188(13)	1282.6(3)
6.18(5)	10.4151(17)	13.682(3)	8.9423(14)	86.36(3)	86.83(2)	89.247(14)	1269.7(4)
7.34(5)	10.354(2)	13.648(3)	8.952(2)	86.20(3)	86.31(2)	89.03(2)	1259.5(5)
7.90(5)	10.322(3)	13.605(5)	8.954(3)	85.74(4)	86.09(3)	89.20(3)	1250.8(7)
8.26(5)	10.313(3)	13.587(5)	8.955(3)	85.67(4)	85.98(3)	89.16(3)	1248.1(7)
7.23(5) (rev)	10.344(2)	13.631(5)	8.963(3)	85.94(4)	86.13(3)	89.21(3)	1257.7(7)
4.65(5) (rev)	10.448(2)	13.751(3)	8.9760(15)	86.64(3)	87.14(3)	89.42(2)	1285.6(4)
2.95(5) (rev)	10.4942(13)	13.765(2)	9.0056(9)	86.050(16)	86.742(15)	89.468(11)	1295.7(3)
1.23(5) (rev)	10.4120(12)	14.0328(13)	8.9681(7)				1310.3(2)
P_{amb} (rev)	10.3917(12)	14.0991(12)	8.9866(6)				1316.7(2)

TABLE 3B: UNIT-CELL PARAMETERS OF PENTAGONITE AS A FUNCTION OF *P* (POWDER COMPRESSED IN S.O.). REV= PATTERNS COLLECTED UPON *P* RELEASE.

Pentagonite (s.o.)							
P (GPa)	*a* (Å)	*b* (Å)	*c* (Å)	α (°)	β (°)	γ (°)	*V* (Å^3)
P_{amb}	10.3848(19)	14.0914(19)	8.9902(10)				1315.6(3)
0.25(5)	10.376(2)	14.063(2)	8.9738(10)				1309.5(4)
0.64(5)	10.362(2)	14.034(2)	8.9601(11)				1303.0(4)
1.27(5)	10.305(3)	14.048(3)	8.8842(16)				1286.1(5)
1.71(5)	10.2559(12)	14.019(3)	8.8521(14)	89.212(18)	89.508(12)	89.767(15)	1272.5(4)
2.15(5)	10.2297(14)	14.013(3)	8.8338(12)	89.155(18)	89.503(13)	89.617(17)	1266.1(4)
2.75(5)	10.175(3)	14.025(5)	8.816(3)	88.82(4)	89.46(2)	89.572(12)	1271.9(4)
4.03(5)	10.120(4)	13.988(7)	8.803(6)	88.15(5)	88.96(5)	89.19(5)	1245.1(12)
4.57(5)	10.098(13)	13.97(2)	8.76(2)	88.3(3)	88.75(16)	89.11(19)	1234(4)
5.55(5)	10.053(6)	13.901(12)	8.696(7)	88.35(10)	88.82(5)	89.31(7)	1214.4(16)
6.20(5)	10.048(7)	13.794(17)	8.676(9)	88.30(10)	88.63(6)	89.26(4)	1201(2)
6.94(5)	10.024(11)	13.83(3)	8.660(15)	88.24(17)	88.65(11)	89.18(10)	1200(3)
7.51(5)	10.034(5)	13.797(12)	8.471(6)	87.30(6)	88.57(4)	89.36(5)	1171.0(14)
8.35(5)	10.003(12)	13.78(3)	8.456(16)	87.22(16)	88.68(15)	89.48(19)	1164(4)
6.30(5) (rev)	10.004(8)	13.84(2)	8.673(12)	88.07(14)	88.65(9)	89.33(9)	1200(3)
3.50(5) (rev)	10.121(7)	13.979(14)	8.779(7)	88.18(12)	88.81(6)	89.24(9)	1241.1(18)
P_{amb} (rev)	10.3914(11)	14.0967(17)	8.9862(18)				1316.7(2)

TABLE 4: HYDROGEN-BOND DISTANCES (Å) AT P_{amb}, 1.08(5), 3.27(5) AND 6.45(5) GPa FOR CAVANSITE POWDER COMPRESSED IN S.O.

		Danisi et al. [20]	P_{amb} in DAC	1.08(3) GPa	3.27(4) GPa	6.45(5) GPa
Species	Hydrogen bond	D…A	D…A	D…A		
H_2O	O9-H9a...O6	3.033(4)	3.02(8)	3.11(5)	3.30(5)	3.39(8)
H_2O	O7-H7a...O9	2.871(4)	2.83(5)	2.84(4)	2.90(4)	2.71(5)
H_2O	O8-H8...O3	3.564(2)	3.55(6)	3.32(4)	3.06(5)	3.09(6)
H_2O	O7-H7b...O5	2.897(2)	2.98(5)	2.83(4)	2.95(4)	3.03(5)

D:donor; A: acceptor.

SUPPLEMENTARY MATERIAL: TABLES S5 AND S6

TABLE S5a: ATOMIC COORDINATES AND U_{iso} (Å^2) VALUES FOR CAVANSITE AT P_{amb} IN AIR.

Site	*Atom*	*x*	*y*	*z*	U_{iso}
V	V	0.0248(3)	0.25	0.0970(3)	0.0061(10)
Ca	Ca	-0.3826(4)	0.75	-0.0801(4)	0.0090(12)
Si1	Si	-0.1822(4)	0.5338(3)	-0.0955(4)	0.0075(7)
Si2	Si	-0.1071(4)	0.4552(3)	0.1848(4)	0.0075(7)
O1	O	-0.1783(8)	0.6493(4)	-0.0864(8)	0.0113(11)
O2	O	-0.0914(9)	0.3418(5)	0.2086(7)	0.0113(11)
O3	O	-0.2071(7)	0.4804(6)	0.0498(7)	0.0113(11)
O4	O	-0.0414(8)	0.4917(6)	-0.1684(7)	0.0113(11)
O5	O	-0.3185(8)	0.4922(5)	-0.1833(7)	0.0113(11)
O6	O	-0.0441(9)	0.25	-0.0494(9)	0.0113(11)
O7	H_2O	-0.4731(7)	0.8825(4)	0.0590(7)	0.033(2)
O8	H_2O	-0.6392(10)	0.75	-0.1196(10)	0.033(2)
O9	H_2O	-0.2817(11)	0.75	0.1937(10)	0.033(2)

TABLE S5b: ATOMIC COORDINATES AND U_{iso} (Å^2) VALUES FOR CAVANSITE IN S.O. AT 1.08(5) GPa.

Site	*Atom*	*x*	*y*	*z*	U_{iso}
V	V	0.0284(16)	0.25	0.1033(17)	0.036(7)
Ca	Ca	-0.3797(18)	0.75	-0.079(2)	0.082(8)
Si1	Si	-0.190(2)	0.5393(12)	-0.0947(19)	0.031(4)
Si2	Si	-0.1018(16)	0.4461(14)	0.1785(17)	0.031(4)
O1	O	-0.181(2)	0.6518(14)	-0.078(3)	0.050(8)
O2	O	-0.077(3)	0.3416(16)	0.224(3)	0.050(8)
O3	O	-0.203(3)	0.467(2)	0.045(2)	0.050(8)
O4	O	-0.043(3)	0.4825(16)	-0.159(3)	0.050(8)
O5	O	-0.316(3)	0.4945(19)	-0.196(3)	0.050(8)
O6	O	-0.039(4)	0.25	-0.042(2)	0.050(8)
O7	H_2O	-0.471(3)	0.8757(19)	0.079(3)	0.115(11)
O8	H_2O	-0.644(5)	0.75	-0.104(5)	0.115(11)
O9	H_2O	-0.268(4)	0.75	0.202(5)	0.115(11)

TABLE S5c: ATOMIC COORDINATES AND U_{iso} (Å^2) VALUES FOR CAVANSITE IN S.O. AT 3.27(5) GPa.

Site	*Atom*	*x*	*y*	*z*	U_{iso}
V	V	0.024(2)	0.25	0.127(2)	0.036
Ca	Ca	-0.367(3)	0.75	-0.069(3)	0.082
Si1	Si	-0.188(3)	0.5199(18)	-0.104(3)	0.031
Si2	Si	-0.123(3)	0.470(2)	0.189(2)	0.031
O1	O	-0.163(3)	0.642(2)	-0.069(4)	0.050
O2	O	-0.098(4)	0.349(2)	0.231(3)	0.050
O3	O	-0.201(4)	0.459(3)	0.042(3)	0.050
O4	O	-0.033(3)	0.482(3)	-0.155(3)	0.050
O5	O	-0.301(3)	0.456(3)	-0.197(3)	0.050
O6	O	-0.050(4)	0.25	-0.019(2)	0.050
O7	H_2O	-0.446(4)	0.883(2)	0.056(3)	0.050
O8	H_2O	-0.644(6)	0.75	-0.074(6)	0.050
O9	H_2O	-0.253(5)	0.75	0.205(5)	0.050

TABLE S5d: ATOMIC COORDINATES AND U_{iso} (Å^2) VALUES FOR CAVANSITE IN S.O. AT 6.45(5) GPa.

Site	*Atom*	*x*	*y*	*z*	U_{iso}
V	V	0.037(3)	0.25	0.149(3)	0.036
Ca	Ca	-0.353(3)	0.75	-0.075(3)	0.082
Si1	Si	-0.184(4)	0.504(2)	-0.100(3)	0.031
Si2	Si	-0.121(4)	0.487(2)	0.206(4)	0.031
O1	O	-0.168(4)	0.634(2)	-0.087(5)	0.050
O2	O	-0.112(4)	0.356(2)	0.204(5)	0.050
O3	O	-0.198(5)	0.470(3)	0.060(3)	0.050
O4	O	-0.031(4)	0.469(3)	-0.157(4)	0.050
O5	O	-0.293(4)	0.434(2)	-0.192(4)	0.050
O6	O	-0.040(7)	0.25	0.003(4)	0.050
O7	H_2O	-0.425(5)	0.883(3)	0.065(5)	0.050
O8	H_2O	-0.648(8)	0.75	-0.072(7)	0.050
O9	H_2O	-0.260(8)	0.75	0.216(7)	0.050

TABLE S6: INTERATOMIC DISTANCES (Å) AND T-O-T ANGLES (°) OF CAVANSITE IN S.O. AT P_{amb}, 1.08(5), 3.27(5) AND 6.45(5) GPa.

Ca coordination	P_{amb} capillary	1.08(5) GPa	3.27(5) GPa	6.45(5) GPa
Ca-O1 (2×)	2.404(7)	2.32(2)	2.39(3)	2.27(3)
Ca-O2 (2×)	2.434(6)	2.33(2)	2.35(2)	2.55(4)
Ca-O7 (2×)	2.429(7)	2.456(3)	2.22(4)	2.25(5)
Ca-O8	2.504(10)	2.54(4)	2.66(5)	2.81(7)
Ca-O9	2.855(10)	2.95(4)	2.90(4)	2.98(6)
Mean	2.487	2.461	2.435	2.492
V coordination	P_{amb} capillary	1.08(5) GPa	3.27(5) GPa	6.45(5) GPa
V-O1 (2×)	2.024(7)	1.990(12)	1.996(4)	1.9998(16)
V-O2 (2×)	2.007(7)	1.981(12)	1.998(4)	1.9998(16)
V-O6	1.582(9)	1.565(16)	1.601(6)	1.60(2)
Mean	1.929	1.901	1.918	1.920
Si1 coordination	P_{amb} capillary	1.08(5) GPa	3.27(5) GPa	6.45(5) GPa
Si1-O1	1.581(6)	1.527(14)	1.614(6)	1.620(2)
Si1-O3	1.619(7)	1.680(14)	1.633(6)	1.621(2)
Si1-O4	1.638(7)	1.721(15)	1.644(6)	1.622(2)
Si1-O5	1.671(7)	1.671(15)	1.632(6)	1.621(2)
Mean	1.627	1.650	1.631	1.621
Si2 coordination	P_{amb} capillary	1.08(5) GPa	3.27(5) GPa	6.45(5) GPa
Si2-O2	1.576(7)	1.495(15)	1.620(6)	1.620(2)
Si2-O3	1.673(7)	1.654(15)	1.628(6)	1.621(2)
Si2-O4	1.613(7)	1.702(15)	1.647(6)	1.623(2)
Si2-O5	1.643(8)	1.668(16)	1.637(6)	1.621(2)
Mean	1.626	1.630	1.633	1.621
T-O-T angles	P_{amb} capillary	1.08(5) GPa	3.27(5) GPa	6.45(5) GPa
Si1 O3 Si2	134.7(5)	134(2)	134(3)	141(3)
Si1 O4 Si2	128.4(5)	117.2(15)	141(3)	144(3)
Si1 O5 Si2	126.9(4)	127.2(17)	113(2)	110(2)
V-O-T angles	P_{amb} capillary	1.08(5) GPa	3.27(5) GPa	6.45(5) GPa
V O1 Si1	133.9(5)	133.4(17)	135(2)	139 (3)
V O2 Si2	126.0(4)	119.5(16)	123.6(18)	134(2)
L/S ratio	P_{amb} capillary	1.08(5) GPa	3.27(5) GPa	6.45(5) GPa
	1.74	1.63	1.50	1.25

SUPPLEMENTARY MATERIAL: TABLES S7 AND S8

TABLE S7a1: ATOMIC COORDINATES AND U_{iso} (Å^2) VALUES FOR PENTAGONITE AT P_{amb} IN AIR.

Site	*Atom*	*x*	*y*	*z*	U_{iso}
V	V	-0.02201(6)	0	-0.11121(9)	0.00934(19)
Ca	Ca	0.24003(7)	0	-0.32387(12)	0.0106(2)
Si1	Si	0.12754(7)	0.20594(6)	-0.14333(10)	0.0079(2)
Si2	Si	0.12350(8)	0.20719(6)	-0.48249(11)	0.0065(2)
O1	O	0.12231(16)	0.09324(14)	-0.1405(3)	0.0096(6)
O2	O	0.11886(19)	0.09416(14)	-0.4913(3)	0.0110(6)
O3	O	0.2534(2)	0.2461(2)	-0.0658(2)	0.0167(5)
O4	O	0.0038(2)	0.25446(13)	-0.0628(2)	0.0125(5)
O5	O	0.12515(17)	0.24565(13)	-0.3153(3)	0.0128(4)
O6	O	-0.0910(3)	0	-0.2700(4)	0.0215(9)
O7	H_2O	0.4005(2)	0.11866(16)	-0.2943(4)	0.0452(9)
O8	H_2O	0.6213(4)	0	-0.0581(4)	0.0527(14)
O9	H_2O	0.3497(5)	0	0.0506(8)	0.155(4)

TABLE S7a2: ANISOTROPIC DISPLACEMENT PARAMETERS FOR PENTAGONITE AT P_{amb} IN AIR.

Site	U_{11}	U_{22}	U_{33}	U_{23}	U_{13}	U_{12}
V	0.0089(3)	0.0071(3)	0.0121(5)	0	0.0022(4)	0
Ca	0.0097(3)	0.0096(4)	0.0125(6)	0	-0.0007(5)	0
Si1	0.0065(4)	0.0091(5)	0.0081(7)	-0.0008(4)	-0.0002(4)	-0.0007(3)
Si2	0.0067(4)	0.0067(5)	0.0062(6)	0.0008(4)	-0.0002(4)	-0.0006(4)
O1	0.0102(9)	0.0081(12)	0.0106(17)	0.0012(11)	0.0005(12)	-0.0015(8)
O2	0.0115(10)	0.0106(13)	0.0110(16)	0.0000(13)	-0.0054(11)	-0.0012(9)
O3	0.0137(8)	0.0172(11)	0.0193(16)	-0.0030(9)	-0.0066(9)	-0.0016(8)
O4	0.0119(8)	0.0068(9)	0.0188(15)	-0.0007(10)	0.0061(9)	-0.0002(11)
O5	0.0223(8)	0.0115(9)	0.0046(11)	0.0006(12)	-0.0011(13)	-0.0003(8)
O6	0.0246(16)	0.0251(19)	0.015(3)	0	-0.0029(15)	0
O7	0.0358(13)	0.0440(16)	0.056(2)	-0.0179(17)	0.0183(17)	-0.0236(11)
O8	0.049(2)	0.069(3)	0.040(4)	0	-0.024(2)	0
O9	0.054(3)	0.137(7)	0.275(11)	0	-0.010(4)	0

TABLE S7b: ATOMIC COORDINATES AND U_{iso} (Å^2) VALUES FOR PENTAGONITE IN M.E.W. AT 1.51(5) GPa.

Site	*Atom*	*x*	*y*	*z*	U_{iso}
V	V	-0.02051(18)	0	-0.1094(2)	0.0145(6)
Ca	Ca	0.2433(2)	0	-0.3206(4)	0.0159(7)
Si1	Si	0.1275(2)	0.2035(5)	-0.1433(2)	0.0090(4)
Si2	Si	0.1232(3)	0.2059(5)	-0.4838(2)	0.0090(4)
O1	O	0.1222(5)	0.0895(6)	-0.1365(8)	0.0157(7)
O2	O	0.1172(6)	0.0915(7)	-0.4876(7)	0.0157(7)
O3	O	0.2527(7)	0.2482(13)	-0.0684(6)	0.0157(7)
O4	O	0.0031(6)	0.2541(8)	-0.0628(6)	0.0157(7)
O5	O	0.1257(4)	0.2445(8)	-0.3139(5)	0.0157(7)
O6	O	-0.0823(7)	0	-0.2731(6)	0.0157(7)
O7	H_2O	0.3946(5)	0.1185(10)	-0.2997(9)	0.028(2)
O8	H_2O	0.6243(9)	0	-0.0634(12)	0.049(4)
O9	H_2O	0.3270(19)	0	0.148(4)	0.220(12)
O10	H_2O	0.3694(16)	0	-0.0482(19)	0.122(13)
Note: the refined site occupancy factor of O10 is 0.94(3)					

TABLE S7c: ATOMIC COORDINATES AND U_{iso} ($Å^2$) VALUES FOR PENTAGONITE IN M.E.W. AT 2.04(5) GPa.

Site	*Atom*	*x*	*y*	*z*	U_{iso}
V	V	-0.01849(18)	0	-0.1086(3)	0.0126(6)
Ca	Ca	0.2444(2)	0	-0.3179(5)	0.0172(7)
Si1	Si	0.1281(2)	0.2022(5)	-0.1436(2)	0.0086(4)
Si2	Si	0.1236(3)	0.2060(5)	-0.4846(2)	0.0086(4)
O1	O	0.1229(5)	0.0882(6)	-0.1374(9)	0.0154(7)
O2	O	0.1173(6)	0.0918(7)	-0.4895(9)	0.0154(7)
O3	O	0.2527(7)	0.2455(14)	-0.0658(9)	0.0154(7)
O4	O	0.0022(6)	0.2533(8)	-0.0663(8)	0.0154(7)
O5	O	0.1263(4)	0.2452(8)	-0.3135(6)	0.0154(7)
O6	O	-0.0795(7)	0.0000	-0.2740(7)	0.0154(7)
O7	H_2O	0.3923(5)	0.1202(10)	-0.2987(9)	0.0200(19)
O8	H_2O	0.6248(10)	0	-0.0580(12)	0.046(5)
O9	H_2O	0.3211(19)	0	0.171(5)	0.186(9)
O10	H_2O	0.3718(13)	0	-0.0552(15)	0.075(9)
Note: the refined site occupancy factor of O10 is 0.96(3).					

TABLE S8: INTERATOMIC DISTANCES (Å) AND T-O-T ANGLES (°) OF PENTAGONITE AT P_{AMB}, 1.51(5), AND 2.04(5) GPA.

Ca coordination	P_{amb} air	1.51(5) GPa	2.04(5) GPa
Ca-O1 (2×)	2.428(2)	2.421(8)	2.390(9)
Ca-O2 (2×)	2.360(2)	2.363(8)	2.396(9)
Ca-O7 (2×)	2.364(2)	2.295(11)	2.289(11)
Ca-O8	2.544(4)	2.568(10)	2.535(11)
Ca-O10		2.764(17)	2.689(13)
Mean	2.407	2.436	2.422
V coordination	P_{amb} air	1.51(5) GPa	2.04(5) GPa
V-O1 (2×)	2.001(2)	1.957(7)	1.938(7)
V-O2 (2×)	1.975(2)	1.959(7)	1.959(8)
V-O6	1.593(3)	1.597(6)	1.604(6)
Mean	1.909	1.886	1.880
Si1 coordination	P_{amb} air	1.51(5) GPa	2.04(5) GPa
Si1-O1	1.582(2)	1.602(7)	1.601(7)
Si1-O3	1.579(2)	1.591(6)	1.589(6)
Si1-O4	1.619(2)	1.640(6)	1.643(6)
Si1-O5	1.641(3)	1.629(6)	1.630(7)
Mean	1.605	1.616	1.616
Si2 coordination	P_{amb} air	1.51(5) GPa	2.04(5) GPa
Si2-O2	1.588(2)	1.605(7)	1.603(7)
Si2-O3	1.615(3)	1.627(6)	1.625(6)
Si2-O4	1.640(2)	1.636(7)	1.637(7)
Si2-O5	1.594(3)	1.612(6)	1.621(7)
Mean	1.626	1.620	1.622
T-O-T angles	P_{amb} air	1.51(5) GPa	2.04(5) GPa
Si1 O3 Si2	176.3(2)	177.1(5)	177.5(12)
Si1 O4 Si2	131.29(12)	129.9(7)	130.2(7)
Si1 O5 Si2	140.37(12)	139.7(8)	138.4(8)
V-O-T angles	P_{amb} air	1.51(5) GPa	2.04(5) GPa
V O1 Si1	132.89(11)	132.2(4)	131.9(4)
V O2 Si2	135.23(14)	133.3(4)	133.9(5)